Physics of Fluids ARTICLE pubs.aip.org/aip/pof

Nonlinear resonance mechanisms and cross-order harmonic coupling of deep-water waves excited by a moving pressure field

Cite as: Phys. Fluids 38, 092105 (2026); doi: 10.1063/5.0340422
Submitted: 24 April 2026 · Accepted: 13 August 2026 ·
Published Online: 1 September 2026

View Online Export Citation CrossMark

Danshi Zhao[1] and Shijun Liao[1,2,a)]

AFFILIATIONS

[1]School of Ocean and Civil Engineering, Shanghai Jiao Tong University, Shanghai 200240, China
[2]State Key Laboratory of Ocean Engineering, Shanghai Jiao Tong University, Shanghai 200240, China

[a)]Author to whom correspondence should be addressed: sjliao@sjtu.edu.cn

ABSTRACT

Within the framework of the homotopy analysis method, the method of directly defining inverse mapping is applied to investigate the strongly nonlinear resonance and cross-order harmonic coupling of deep-water waves excited by a moving pressure field. By directly defining new inverse operators, this analytical framework offers a practical way to handle the small-divisor difficulty encountered in traditional perturbation theories. It does not require the weak-nonlinearity assumption or the scale-separation procedure used in methods such as multiple scales. In the primary resonance region, the nonlinear dispersion of deep-water waves causes the forced-response branches to bend rightward and develop fold bifurcations. An empirical relation is obtained for the moderate-to-strong nonlinear regime to characterize cross-order coupling in the discrete spectrum. It suggests that the higher-order harmonics of the deviation velocity potential are strongly influenced by adjacent lower-order background-wave components, which act as an important source of parametric excitation through nonlinear steepening. This study elucidates the regularities of discrete spectra and the cross-order evolution mechanisms of deep-water forced waves under resonance modes.

Published under an exclusive license by AIP Publishing. https://doi.org/10.1063/5.0340422

02 September 2026 00:36:10

I. INTRODUCTION

Wave generation and resonance induced by a moving pressure disturbance on a free surface represent a classical fluid mechanics problem with extensive applications in naval architecture and meteorological oceanography, exhibiting pronounced nonlinear forced resonance characteristics when the load velocity approaches the characteristic wave speed. For fundamental wave-making features, Doctors and Sharma[1] and Maki *et al.*[2] investigated the nonlinear wave resistance of air-cushion vehicles (ACVs), while a pressure disturbance translating at transcritical speeds can periodically generate upstream-propagating solitary waves in shallow channels, as demonstrated by Akylas,[3] Ertekin *et al.*,[4] Wu,[5] and Ersan and Beji.[6] More specifically, Doctors and Dagan[7] systematically compared several nonlinear wave-resistance theories for a two-dimensional pressure distribution moving over water of finite depth, demonstrating the importance of nonlinear free-surface effects in moving pressure wave generation. This moving-load formulation has been successfully extended to hydroelastic waves in ice-covered water,[8,9] flexural-gravity waves,[10–13] and resonant internal-wave generation over topography in stratified fluids.[14] When the forcing possesses a coherent spatiotemporal structure, this velocity-matching resonance becomes dominant: Phillips[15] established a resonance mechanism for wind-wave generation, which later inspired coherent local pressure distributions for numerical wave generation.[16] In nature, atmospheric periodic pressure waves translating near the local shallow-water wave speed trigger Proudman resonance over seabed topography, severely amplifying meteotsunamis,[17,18] a phenomenon further examined numerically by Kakinuma and Kosugi.[19] Similarly, single-file ship formations can be viewed as interacting periodic moving disturbances whose wave-field interference significantly modifies the overall wave pattern and wave drag.[20] Therefore, studying the resonance theory of forced traveling waves has broad significance.

Nonlinear forced waves excited by a moving pressure field have long attracted significant attention in theoretical fluid mechanics. In shallow-water and finite-depth regimes, the resonance mechanism is typically governed by the forced Korteweg–de Vries (fKdV) framework, with prior literature predominantly focusing on transcritical soliton radiation, the macroscopic evolution of long waves, and

Published under an exclusive license by AIP Publishing

localized steepening characteristics of steady-state solutions.[3,5,19,21] More directly related to pressure-induced resonance, Akylas[22] investigated nonlinear water waves excited by a moving pressure distribution oscillating near the resonant frequency. Within a weakly nonlinear finite-depth framework, the bounded resonant response was shown to be asymptotically governed by a forced nonlinear Schrödinger equation. Conversely, the nonlinear evolution of free-surface waves in deep water is inherently dictated by high-order wave–wave interactions and discrete energy cascades,[23,24] with relative motion significantly altering the resonance pathways.[25] Although extensive efforts have been made to explore the spectral evolution of source-free free waves under weak-nonlinearity assumptions[26,27] as well as the discrete spectra of steady-state wave–wave nonlinear resonance in the absence of external loads,[28,29] conventional studies on forced waves under a deterministic forcing, such as a moving pressure field, still treat the system as a macroscopic unified entity,[30] largely centering on global surface profile characteristics,[31–33] complex bifurcation behaviors,[8,9] or semi-analytical numerical wave-making techniques.[16]

Regarding the harmonic structure of gravity waves under surface-pressure forcing, Zdyrski and Feddersen[34] derived weakly nonlinear solutions for progressive waves in deep to intermediate water and showed that prescribed wave-coherent pressure distributions can modify the harmonic phase and relative harmonic amplitude of the wave profile. Nevertheless, the modal dynamics of strongly nonlinear steady deep-water waves maintained by a periodic moving pressure field has not been examined in comparable detail. In particular, how the directly forced fundamental mode and the nonlinearly generated higher-order harmonics evolve and couple across the multivalued response branches near primary resonance remains insufficiently understood.

To address this gap, the present work focuses on a periodic moving pressure field and examines the modal coupling characteristics in steady-state deep-water forced resonant waves from a discrete spectral perspective. This study provides more insight into nonlinear wave resonance under external forcing and may help support future efforts in the control and spectral characterization of deep-water wave fields.

We consider a two-dimensional (2D) steady forced wave field excited by a surface load translating at a constant velocity in deep water. In a coordinate system (x, y) moving with the wave, where the x-axis is positive in the direction of wave propagation and the y-axis points vertically upward from the still-water level, the fluid is assumed to be incompressible, inviscid, and free of surface tension. This boundary value problem can be described by a dimensionless velocity potential ϕ that satisfies the Laplace equation:

$$\nabla^2\phi = 0 \quad \text{for } (x, y) \in \Omega, \tag{1}$$

where ϕ is the dimensionless velocity potential, $\Omega = \{(x, y) | -\infty < x < +\infty, -\infty < y < \xi(x)\}$, and ξ represents the dimensionless surface elevation, subject to the surface boundary conditions,

$$U^2\phi_{xx} + \phi_y + \frac{1}{2}\nabla\phi\nabla(\nabla\phi\nabla\phi) - 2U\nabla\phi\nabla\phi_x + (U - \phi_x)P_x = 0 \quad \text{at } y = \xi(x), \tag{2}$$

$$\xi(x) = U\phi_x - \frac{1}{2}\nabla\phi\nabla\phi + P \quad \text{at } y = \xi(x), \tag{3}$$

where the subscripts denote partial derivatives in the respective directions. In the moving coordinate system (x, y), the dimensionless external load with spatial periodicity is in the form $P = P_a \cos(x)$. U represents the dimensionless translational velocity of the external forcing. Additionally, the bottom boundary condition

$$\lim_{y\to-\infty} \frac{\partial\phi}{\partial y} = 0, \tag{4}$$

must be considered.

In solving forced waves, conventional perturbation methods inevitably encounter the severe "small-divisor problem."[35] As noted by Poincaré[36] and originally identified by Delaunay,[37] this serves as a fundamental dynamical obstacle for nearly integrable systems under resonance conditions.[36,38] For the deep-water forced wave system governed by Eqs. (1)–(4), the first-order perturbation solution $\phi_{pr} = -Ue^y P_x/(1 - U^2)$ as well as all subsequent higher-order corrections inherently contains denominators of the form $1 - U^2$. As the primary resonance condition is approached ($U \to 1$), these denominators vanish and precipitate the divergence of the perturbation series, a phenomenon most prevalent in perturbation theory.[39]

To circumvent this theoretical barrier, various analytical and numerical techniques have been developed; however, each possesses inherent limitations when applied to strongly nonlinear forced resonance. The method of multiple scales (MMS) eliminates secular terms by introducing slow temporal and spatial scales to absorb resonant forcing effects.[40] Nevertheless, it strictly relies on a weak-nonlinearity assumption, and its algebraic complexity grows exponentially as higher-order expansions are pursued.[41] The high-order spectral method (HOSM)[42] is well-suited to nonlinear transient evolution, yet it cannot directly provide closed-form analytical representations for broad parameter scans, and its efficiency is constrained when tracing steady-state periodic solutions or capturing unstable solution branches. The harmonic balance method (HBM) reduces the dependence on small-parameter assumptions, but high-order truncation in strongly nonlinear regimes yields an extensive system of algebraic equations that is highly sensitive to initial guesses and requires meticulous step-size control during parameter continuation.[43] In addition, HBM is a numerical method and cannot provide low-order analytical expressions for the parameters, making it less efficient than analytical approximation methods in parameter sweeps.

Given the aforementioned limitations regarding algebraic complexity, convergence, and analytical representation, the present study employs the Homotopy Analysis Method (HAM)[28,44–54] and its recent advancement,[55,56] the Method of Directly Defining inverse Mapping (MDDiM). As an approximate analytical tool tailored for strongly nonlinear problems, MDDiM avoids the need for traditional scale analysis or multi-scale expansion procedures. Instead, by virtue of its flexibility in selecting linear operators, it offers a way to regularize the singular behavior associated with small denominators, thereby producing convergent steady-state analytical approximations for exploring the mechanisms of deep-water forced resonance. Based on the analytical framework of MDDiM, this paper develops two auxiliary linear operators, extending the use of the MDDiM method for small-divisor problems from ordinary differential equations to partial differential equations.

We illustrate in Sec. II how to avoid the "small-divisor problem" by means of MDDiM within the HAM framework. Results and

02 September 2026 00:36:10

Published under an exclusive license by AIP Publishing

discussion about primary resonance are given in Sec. III, and concluding remarks are given in Sec. IV.

II. MATHEMATICAL APPROACH

As discussed in Sec. I, the root cause of the small-denominator crisis in the traditional perturbation method lies in its dependence on small physical parameters and its inability to freely choose the linear operator. This leads to the generation of very small denominators under resonance conditions for certain parameters, which severely disrupts the convergence of the perturbation series. To overcome this deficiency, the method of directly defining inverse mapping (MDDiM)[55] is introduced within the unified framework of the homotopy analysis method (HAM). The core feature of this approach is that it neither relies on small physical parameters nor requires an explicit expression of the auxiliary linear operator; instead, the inverse mapping between basis functions is directly defined, thereby avoiding the singularities induced by resonance.

In the following, we apply the MDDiM to solve the system of governing Eqs. (1)–(4). The velocity potential $\phi(x,y)$ satisfying the Laplace Eq. (1) and the bottom boundary condition (4), along with the corresponding wave surface elevation $\xi(x)$, can be expressed in the following expanded forms of basis function series:

$$\phi = \sum_{j=1}^{+\infty} \alpha_j e^{jy} \sin(jx), \tag{5}$$

$$\xi = \sum_{j=0}^{+\infty} \sigma_j \cos(jx), \tag{6}$$

where α_j and σ_j are the expansion coefficients to be determined. The selection of these basis functions is directly motivated by the physical characteristics of the present deep-water wave problem. Specifically, the exponential term e^{jy} satisfies the Laplace equation, while ensuring that the velocity potential decays exponentially with depth, consistent with the deep-water boundary condition. The trigonometric functions $\sin(jx)$ and $\cos(jx)$ reflect the spatial periodicity of the two-dimensional forced gravity-wave system and constitute the natural Fourier basis for steady periodic waves in the horizontal direction. Consequently, the adopted basis functions simultaneously satisfy the governing equation, the far-field boundary condition, and the spatial periodicity of the forced wave system.

To construct a continuous deformation between the initial guess and the exact solution, we introduce the homotopy embedding parameter $q \in [0,1]$. We then construct two continuous mappings depending on q, namely, the homotopy velocity potential mapping $\Phi(x,y,q)$ and the homotopy wave surface elevation mapping $\Theta(x,q)$ (refer to the supplementary material). Let ϕ_0 and ξ_0 denote the initial approximations for the velocity potential and free-surface elevation. With the convergence-control parameters set as $h_\phi = h_\xi = h$, the zeroth-order deformation equations are constructed as follows:

$$(1-q)\mathscr{L}_\phi\left[\Phi(x,y,q)-\phi_0\right] = hq\mathscr{N}_\phi\left[\Phi(x,y,q)\right] \quad \text{at } y=\Theta(x,q), \tag{7}$$

$$(1-q)\mathscr{L}_\xi\left[\Theta(x,q)-\xi_0\right] = hq\mathscr{N}_\xi\left[\Phi(x,y,q),\Theta(x,q)\right] \quad \text{at } y=\Theta(x,q), \tag{8}$$

where $\mathscr{L}_\phi$ and $\mathscr{L}_\xi$ are auxiliary linear operators satisfying $\mathscr{L}_\phi[0] = \mathscr{L}_\xi[0] = 0$, and $\mathscr{N}_\phi$ and $\mathscr{N}_\xi$ are the original nonlinear operators corresponding to the left-hand sides of the original governing Eqs. (2) and (3). When $q=0$, the equations degenerate to the initial guesses ϕ_0 and ξ_0; when $q=1$, they become identical to the original nonlinear governing equations, yielding the exact solutions $\phi(x,y)$ and $\xi(x)$.

As q increases from 0 to 1, $\Phi(x,y,q)$ and $\Theta(x,q)$ undergo continuous deformations from the initial guesses to the exact solutions. Expanding Φ and Θ as Maclaurin series with respect to q and setting $q=1$ yields the final homotopy series solutions:

$$\phi(x,y) = \phi_0(x,y) + \sum_{i=1}^{+\infty} \phi_i(x,y), \tag{9}$$

$$\xi(x) = \sum_{i=1}^{+\infty} \xi_i(x), \tag{10}$$

where ϕ_i and ξ_i represent the ith order deformation (components) of the velocity potential and wave surface elevation, respectively, whose convergence radius and rate are determined by the convergence-control parameter h.

To solve the equations on the unknown free surface, the boundary conditions must be expanded at the mean water level $y=0$. In this step, the movement of the deformation boundary introduces a sequence of complex convective derivatives, high-order Taylor expansions, and nonlinear combination operators. For the complete, continuous, and step-by-step mathematical derivation of the evolution from the zeroth-order deformation equations to the high-order governing equations, the reader is referred to the supplementary material. By performing an exact Taylor expansion of the homotopy mappings at $y=0$ and setting $\mathscr{L}_\phi = \mathscr{L}$ and $\mathscr{L}_\xi$ as the identity operator, the zeroth-order deformation equations can be transformed into the following ith order deformation equations for successive recurrence:

$$\phi_i|_{y=0} = \chi_i\phi_{i-1}|_{y=0} + \mathscr{L}^{-1}[-\mathscr{T}_i + \chi_i\mathscr{T}_{i-1} + h\mathscr{R}^{\phi}_{i-1}(x)] + \sum_{j=1}^{\mu} A_{i,j}\psi_j(x), \tag{11}$$

$$\xi_i(x) = \chi_i\xi_{i-1}(x) + h\mathscr{R}^{\xi}_{i-1}(x), \quad i=1,2,3\ldots, \tag{12}$$

where χ_i is a step indicator coefficient defined as $\chi_1 = 0$ for $i=1$ and $\chi_i = 1$ for $i>1$. $A_{i,j}$ represents undetermined constants, and $\psi_j = \sin(jx)$ denotes the base functions of the kernel of the linear operator $\mathscr{L}$ (satisfying $\mathscr{L}[\psi_j]=0$) such that the dimension of the kernel space $\ker[\mathscr{L}] = \sum_{j=1}^{\mu} A_{i,j}\psi_j(x)$ is μ. The rigorous mathematical definitions of the high-order nonlinear residual terms $\mathscr{R}^{\phi}_{i-1}(x)$, $\mathscr{R}^{\xi}_{i-1}(x)$, the boundary high-order polynomial correction term $\mathscr{T}_i$, and the high-order evolution operator $\mathscr{D}_i^{(z_n)}$ are provided in Appendix for reference.

In the present problem, the inverse of the linear operator within the traditional perturbation theory develops severe resonance singularities under specific parameter conditions (e.g., when the load moving speed $U \to 1$, the denominator $1/(1-U^2j) \to \infty$), which represents the mathematical essence of the small-divisor problem. To overcome this difficulty, the MDDiM strategy is adopted to directly define the mapping relations between basis functions. We introduce a resonance threshold δ and establish a piecewise inverse mapping

02 September 2026 00:36:10

Published under an exclusive license by AIP Publishing

between the non-resonant space and the resonant kernel space. Here, δ is assumed to be strictly positive, i.e., $\delta > 0$. If $\delta = 0$, only exactly resonant modes satisfying $|1 - U^2 j| = 0$ would be assigned to the resonant kernel space, whereas near-resonant modes with small but nonzero denominators would remain in the non-resonant space. Such a choice would fail to treat any small-divisor terms in the vicinity of resonance and would therefore defeat the purpose of introducing the resonance threshold.

First, a straightforward definition of the operator ($\mathscr{L} = \mathscr{L}_a$) is given by

$$\mathscr{L}_a^{-1}[\sin(jx)] = \begin{cases} \dfrac{1}{j(1-U^2 j)}\sin(jx), & |1-U^2 j| > \delta, \\ \dfrac{1}{j\delta}\sin(jx), & |1-U^2 j| \le \delta. \end{cases} \tag{13}$$

The introduction of the threshold δ merely serves to smooth the iterative path; as shown by the numerical tests in Sec. III, the final converged physical steady-state solution exhibits robust insensitivity to the choice of δ.

To construct a more general scheme suitable for analytical operations, we present another operator definition ($\mathscr{L} = \mathscr{L}_b$), whose core idea is to directly classify all dangerous terms within the resonance band into the kernel space (null space) of the operator:

$$\mathscr{L}_b^{-1}[\sin(jx)] = \frac{1}{j(1-U^2 j)}\sin(jx), \quad |1-U^2 j| > \delta, \tag{14}$$

with its corresponding resonant kernel space defined as

$$\ker[\mathscr{L}_b] = \sum \gamma_j \sin(jx), \quad |1-U^2 j| \le \delta, \tag{15}$$

where the dimension of this resonant kernel space μ (the number of basis functions falling inside the resonance band) is uniquely determined by

$$\mu = \max\left(0, \left\lfloor \frac{1+\delta}{U^2} \right\rfloor - \left\lceil \frac{1-\delta}{U^2} \right\rceil + 1\right), \tag{16}$$

where $\lfloor\cdot\rfloor$ and $\lceil\cdot\rceil$ denote the floor and ceiling functions, respectively.

Based on the operator $\mathscr{L}_b$, the ith order deformation equation is transformed into

$$\phi_i|_{y=0} = \chi_i \phi_{i-1}|_{y=0} + \mathscr{L}_b^{-1}[-\mathscr{T}_i + \chi_i \mathscr{T}_{i-1} + h\mathscr{R}_{i-1}^{\phi}] + \sum_{|1-U^2 j|\le\delta} \gamma_{i,j}\sin(jx), \tag{17}$$

where $\gamma_{i,j}$ are undetermined constants. According to the operator theory in linear algebra, to ensure the validity of the inverse mapping $\mathscr{L}_b^{-1}$, the operand function space (the bracketed terms) must be orthogonal to the kernel space; that is, it must exclude any $\sin(jx)$ terms within the resonance band. Consequently, by expanding the right-hand side and enforcing the coefficients of the resonant terms to vanish, we obtain the condition equations for eliminating the small divisors:

$$S_{i,j} = 0, \quad |1-U^2 j| \le \delta, \tag{18}$$

where $S_{i,j}$ represents the algebraic coefficients corresponding to the resonant basis functions. This system consists of exactly μ equations, matching the number of unknowns $\gamma_{i,j}$ in the kernel space, thereby closing the system. Solving this equation system successively for $\gamma_{i,j}$ allows the analytical calculation of any high-order component ϕ_i without generating any small-denominator terms.

Finally, for computational convenience, the initial approximation of the free surface is chosen as $\xi_0(x) = 0$, so that the undeformed still-water surface is used as the starting surface, and the algebraic complexity of the high-order expansion terms $\mathscr{T}_i$ in the HAM formulation is reduced. The initial approximations serve only as simple estimates and computational starting points and therefore are not required to strictly satisfy the original physical boundary conditions at $q = 0$. The physical coupling between the velocity potential and the free-surface elevation is progressively recovered through the deformation equations, and the original free-surface conditions are fully satisfied at $q = 1$. Unlike the simple choice $\xi_0(x) = 0$, a nonzero initial approximation ϕ_0 is required to retain the modal information needed to identify different nontrivial solution branches. Therefore, ϕ_0 is expressed in a general series form spanning both the non-resonant and resonant spaces:

$$\phi_0 = \sum_{|1-U^2 n|>\delta} \upsilon_{0,n}\, e^{ny}\sin(nx) + \sum_{|1-U^2 j|\le\delta} \gamma_{0,j}\, e^{jy}\sin(jx), \quad 1 \le n, j \le Mn, \tag{19}$$

where $\upsilon_{0,n}$ and $\gamma_{0,j}$ are the undetermined initial coefficients and Mn is the maximum truncation mode number. We define the initial squared residual integral $E_0 = \int_0^{2\pi} \mathscr{N}_{\phi}[\phi_0]^2 dx = \sum S_{0,j}^2$ to quantify the mathematical distance between the initial guess and the exact physical solution.

The selection of the initial solution is thus converted into a constrained optimization problem to minimize the residual E_0 subject to the resonance elimination constraint $S_{0,j} = 0$. Using the Lagrange multiplier method, we construct the Lagrangian function $L_g = \int_0^{2\pi} \mathscr{N}_{\phi}[\phi_0]^2 dx + \sum_{|1-U^2 j|\le\delta} \rho_j S_{0,j}$. Setting the partial derivatives of L_g with respect to all unknown coefficients to zero leads to a system of nonlinear algebraic equations:

$$\begin{cases} \dfrac{\partial L_g}{\partial \upsilon_{0,n}} = 0, & |1-U^2 n| > \delta, \\ \dfrac{\partial L_g}{\partial \gamma_{0,j}} = 0, & |1-U^2 j| \le \delta, \\ S_{0,j} = 0, & |1-U^2 j| \le \delta. \end{cases} \tag{20}$$

Solving this system yields the admissible initial guess solution branches. The concrete numerical techniques and separation strategies for these multiple physical branches are provided in the external supplementary material. According to the convergence theorem of HAM,[57] provided that the parameter h is properly selected to make the high-order residuals vanish, the series solution converged from the MDDiM scheme serves as a physically consistent approximation to the exact solution of the original nonlinear wave equations. For all the detailed derivations in the "Mathematical approach" section, readers can refer to the supplementary material.

III. RESULTS AND DISCUSSION

A. Algorithm validation and assessment

To validate the MDDiM framework, we evaluate its macroscopic accuracy by comparing the calculated dispersion relations with those

02 September 2026 00:36:10

Published under an exclusive license by AIP Publishing

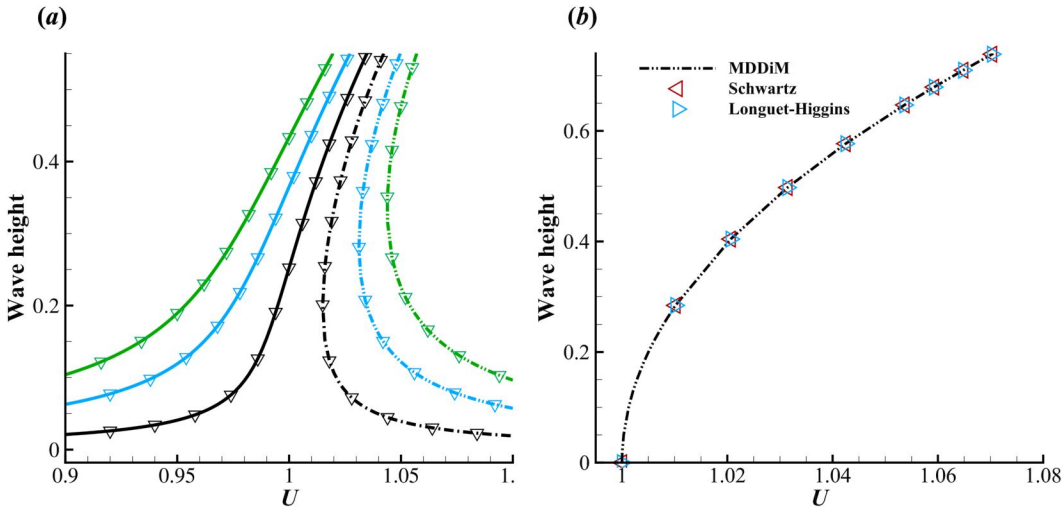

FIG. 1. (a) Using MDDiM and HBM (Harmonic Balance Method) to solve the dispersion relation of wave speed U with respect to wave height. Solid line: MDDiM; triangles: HBM. Black: $P_a = 0.002$; blue: $P_a = 0.006$; green: $P_a = 0.01$. Using the 20th-order solution for MDDiM and 20 Fourier coefficients for HBM, the difference in wave heights obtained by the two methods is less than 0.01%. (b) Variation of the wave height of free-surface Stokes waves with the wave speed U in the zero-forcing limit. The dash-dotted line represents the MDDiM results obtained at $P_a = 0$, while the left- and right-pointing triangles denote the results reported by Schwartz and Longuet-Higgins, respectively. The three sets of results agree well.

obtained from the Harmonic Balance Method (HBM). As shown in Fig. 1(a), under varying external loads, the fully nonlinear response curves from both methods exhibit excellent agreement with a discrepancy below 0.01%. Figure 1(b) presents the Stokes-wave solution obtained by directly applying the MDDiM to the case of $P_a = 0$ and compares it with the results reported by Schwartz[58] and Longuet-Higgins.[59] Excellent agreement is observed among the three sets of results. As shown in Table I and in Tables S12–S16 in the supplementary material, the MDDiM and HBM yield not only nearly identical macroscopic wave heights but also excellent agreement among the Fourier coefficients of different orders in the analytical solutions. This indicates that MDDiM reproduces the multi-valued response topology of the nonlinear forced wave system with high accuracy in the tested cases.

The numerical convergence, stability, and parameter independence of the algorithm are further quantitatively verified. In all tested cases, the sum of squared residuals plummets to the order of 10^{-10} or lower by merely the 15th-order approximation (see Tables S1–S4 in the supplementary material), confirming that the singular-denominator difficulty is effectively handled, and that the iterative scheme converges well in the tested cases. Meanwhile, by solving the forced wave system under strongly nonlinear wave conditions, the applicability of the algorithm under strongly nonlinear conditions is validated (Table S5 in the supplementary material). The convergence-control parameter h exhibits a broad and robust valid region (approximately $-1.7 < h < 0$, see Fig. S1 in the supplementary material). To accommodate strong nonlinearity while maintaining computational convenience, the convergence-control parameter is set to $h = -0.5$ for all cases presented in Figs. 1–8. Any cases using different values of h are explicitly identified in the corresponding tables in the supplementary material. Furthermore, the converged steady-state solutions (Fourier coefficients a_1, a_3, a_5, and a_7) remain highly consistent across different auxiliary linear operators ($\mathscr{L}_a$, $\mathscr{L}_b$) and tuning thresholds ($\delta \in [0.1, 1.1]$) (see Tables S6–S11 in the supplementary material), proving that the final convergence is independent of the chosen iterative pathways (i.e., auxiliary parameters and operators).

TABLE I. Comparison of the Fourier coefficients of the wave surface (a_1, a_3, and a_5) obtained by the MDDiM ($h = -0.85$, $\delta = 0.5$, $\mathscr{L} = \mathscr{L}_b$) and HBM for different wave speeds and solution branches when $P_a = 0.002$.

	a_1		a_3		a_5	
	MDDiM	HBM	MDDiM	HBM	MDDiM	HBM
$U = 0.99$ (Branch 1)	$7.735\,19 \times 10^{-2}$	$7.735\,19 \times 10^{-2}$	$1.859\,32 \times 10^{-4}$	$1.859\,32 \times 10^{-4}$	$1.032\,95 \times 10^{-6}$	$1.032\,95 \times 10^{-6}$
$U = 1.00$ (Branch 1)	$1.254\,29 \times 10^{-1}$	$1.254\,29 \times 10^{-1}$	$8.035\,46 \times 10^{-4}$	8.03546×10^{-4}	$1.201\,57 \times 10^{-5}$	$1.201\,57 \times 10^{-5}$
$U = 1.03$ (Branch 1)	$2.503\,41 \times 10^{-1}$	$2.503\,41 \times 10^{-1}$	$7.543\,78 \times 10^{-3}$	$7.543\,78 \times 10^{-3}$	$5.531\,71 \times 10^{-4}$	$5.531\,71 \times 10^{-4}$
$U = 1.04$ (Branch 2)	$2.577\,18 \times 10^{-1}$	$2.577\,18 \times 10^{-1}$	$8.090\,62 \times 10^{-3}$	$8.090\,62 \times 10^{-3}$	$6.226\,56 \times 10^{-4}$	$6.226\,56 \times 10^{-4}$
$U = 1.06$ (Branch 2)	$3.120\,07 \times 10^{-1}$	$3.120\,07 \times 10^{-1}$	$1.561\,64 \times 10^{-2}$	$1.561\,64 \times 10^{-2}$	$1.532\,99 \times 10^{-3}$	$1.532\,99 \times 10^{-3}$
$U = 1.10$ (Branch 2)	$9.528\,43 \times 10^{-3}$	$9.528\,43 \times 10^{-3}$	$2.397\,33 \times 10^{-7}$	$2.397\,33 \times 10^{-7}$	$1.433\,18 \times 10^{-11}$	$1.433\,18 \times 10^{-11}$

02 September 2026 00:36:10

Published under an exclusive license by AIP Publishing

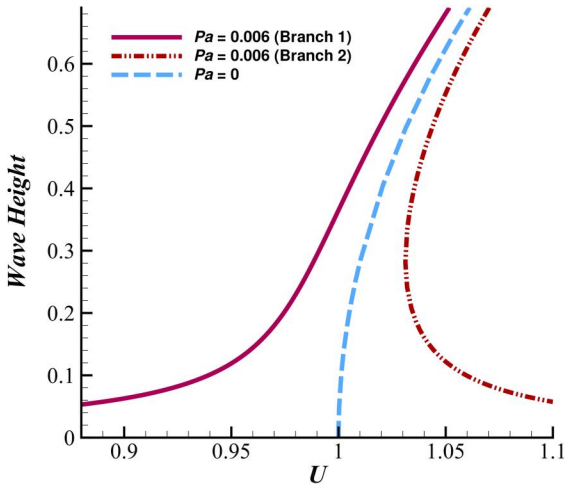

FIG. 2. Variation of the total wave height with the load moving speed U in the primary resonance region. The solid and dash-dotted lines represent the forced-response branches under an external excitation of $P_a = 0.006$, while the dashed line indicates the free wave skeleton curve ($P_a = 0$). The figure demonstrates the nonlinear bending characteristics and the resulting multi-valued solutions.

Such parametric robustness supports the conclusion that MDDiM converges reliably and efficiently to a physically consistent solution.

As shown in Table II, over the range of wave speeds considered, the admissible pressure-amplitude range of the MDDiM is consistently broader than that of the MMS, with the range ratio increasing from 1.5 at $U = 1.02$–7.5 at $U = 1.06$. This indicates that, as the resonant nonlinearity strengthens, the applicability of the MMS becomes increasingly restricted, whereas the MDDiM still yields effectively convergent series solutions over a wider parameter range.

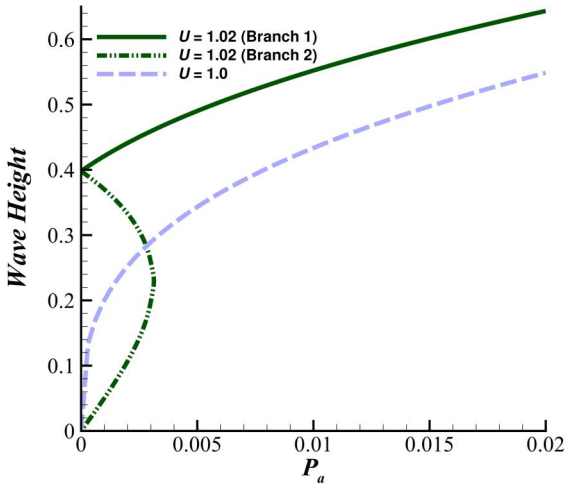

FIG. 3. Variation of the total wave height with the external forcing amplitude P_a in the primary resonance region. The curves compare the amplitude responses at the exact linear resonance speed ($U = 1.0$) and a detuned speed ($U = 1.02$). The detuned case clearly exhibits a limit point (or fold point) leading to the coexistence of multiple steady-state solutions.

TABLE II. Comparison of the admissible pressure-amplitude ranges of the MDDiM and MMS at different wave speeds while ensuring effective convergence of the corresponding series solutions. The range ratio is defined as the ratio of the admissible parameter ranges of P_a for the MDDiM and MMS.

U	MDDiM	MMS	Range ratio
1.02	$0 < P_a < 0.045$	$0 < P_a < 0.030$	1.50
1.03	$0 < P_a < 0.040$	$0 < P_a < 0.025$	1.60
1.04	$0 < P_a < 0.035$	$0 < P_a < 0.015$	2.33
1.05	$0 < P_a < 0.030$	$0 < P_a < 0.010$	3.00
1.06	$0 < P_a < 0.015$	$0 < P_a < 0.002$	7.50

B. Macroscopic forced response and characterization of deviations from the background wave

As a starting point to investigate the nonlinear interaction mechanisms of forced water waves, we first examine the global evolution of the macroscopic physical quantity (total forced wave height) to reveal the bifurcation topologies of the system within primary resonance regions. As shown in Fig. 2, in the vicinity of the primary resonance region ($U \approx 1$), the response curves of the system exhibit strong nonlinear bending characteristics. Due to the nonlinear dispersion relation of deep-water waves, the effective phase speed becomes strongly dependent on the wave steepness, causing the forced-response branches to tilt to the right (toward higher wave speeds). This is consistent with a nonlinear frequency shift analogous to that of a classical hard-spring Duffing oscillator. Under small excitation, the forced wave can essentially be regarded as a nonlinear perturbation of the background wave (unperturbed solution) at the same frequency. In the primary resonance, this connection is intuitively reflected by the fact that the upper and lower response branches (Branch 1 and Branch 2) lie on opposite sides of the unforced free-wave skeleton curve.

The rightward bending of the curves in Fig. 2 provides a geometric interpretation of the multi-valued solutions shown in Fig. 3. In Fig. 3, the response at the exact resonance speed $U = 1.0$ (dashed line) constitutes a critical boundary. When the prescribed wave speed is less than or equal to this critical value, the forced curve smoothly approaches the background wave (unperturbed solution) as the external excitation amplitude P_a decreases, and the system exhibits a monotonic single-valued response. However, for a given detuned speed $U = 1.02 > 1.0$, a vertical line will simultaneously intersect the bent Branch 1 and Branch 2. This geometric mapping relation manifests in Fig. 3 as follows: as the external excitation amplitude increases, the high-wave-height and low-wave-height solutions approach each other and collide at a limit point (or fold point). Once the external forcing exceeds this threshold, the multi-valued topology disappears, and the system may undergo a nonlinear jump.

From the perspective of the wave profiles, as shown in Fig. 4, the forced wave height increases rapidly as the moving speed approaches the resonance region, and the waveform gradually develops a sharp crest and a broad trough, indicating enhanced nonlinearity. At $U = 1.07$, multiple steady solutions with different wave amplitudes coexist under the same parameters, directly illustrating the multivalued branch structure. The waveform on Branch 1 is approximately in

02 September 2026 00:36:10

Published under an exclusive license by AIP Publishing

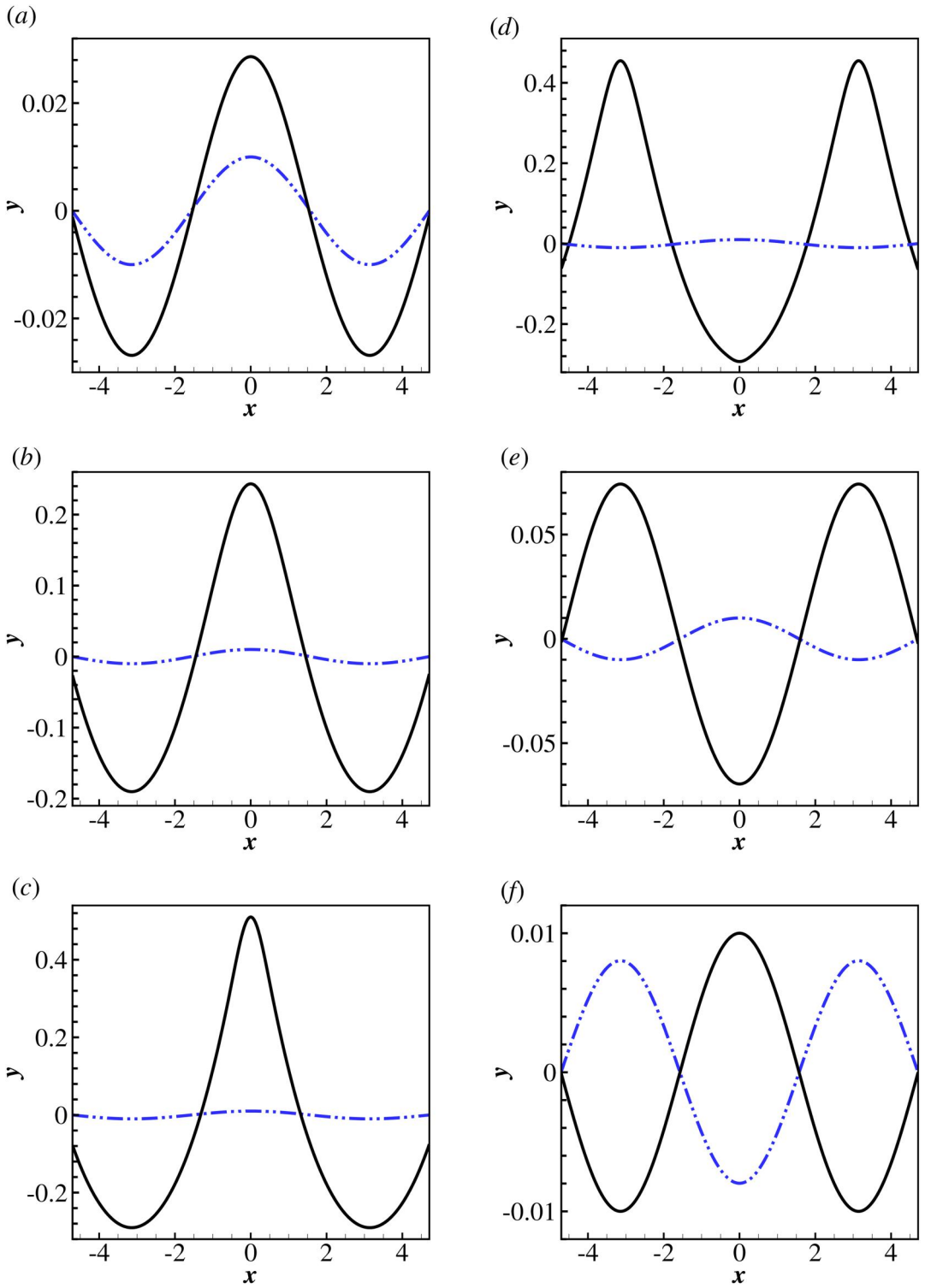

FIG. 4. The waveforms under different load moving speeds when the external pressure load amplitude $P_a = 0.01$. Black solid line: waveform of forced wave; blue dash-dotted line: external load waveform. (a) $U = 0.8$, Branch 1; (b) $U = 1.0$, Branch 1; (c) $U = 1.07$, Branch 1; (d) $U = 1.07$, upper part of Branch 2; (e) $U = 1.07$, lower part of Branch 2; and (f) $U = 1.15$, lower part of Branch 2.

02 September 2026 00:36:10

Published under an exclusive license by AIP Publishing

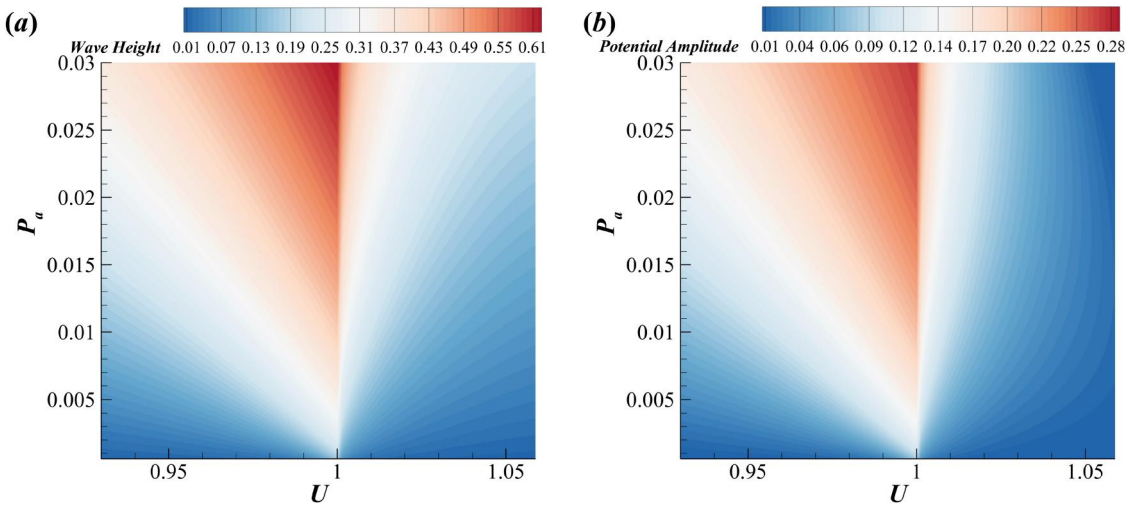

FIG. 5. The variation of wave height and velocity potential amplitude of the deviation response with U and P_a. (a) Wave height and (b) velocity potential amplitude.

phase with the external pressure, whereas that on Branch 2 is out of phase with it. Away from the resonance region, the response on the low-amplitude branch decreases markedly again.

As previously discussed, the total response of the forced wave is the coupled result of the background free-wave field and the forcing effect of the external load. To quantitatively analyze the additional response induced by the moving pressure field on the wave system, we introduce the "deviation" to characterize this process. Mathematically, the deviation $\xi_{excited}$ is defined as the difference between the total forced surface elevation ξ_{total} and the unperturbed solution $\xi_{intrinsic}$ (i.e., the free-wave solution corresponding to homogeneous boundary conditions) at the same phase speed. It characterizes the degree to which the system deviates from the free-wave state under external forcing:

$$\xi_{excited} = \xi_{total} - \xi_{intrinsic}, \tag{21}$$

and

$$\phi_{excited} = \phi_{total} - \phi_{intrinsic}. \tag{22}$$

It should be emphasized that, at a given wave speed U, $\xi_{intrinsic}$ and $\phi_{intrinsic}$ are uniquely determined by the exact nonlinear Stokes free-wave solution satisfying the homogeneous boundary conditions.

Based on the definition of the deviation in Eqs. (21) and (22), Fig. 5 illustrates the evolution of the surface elevation and velocity potential amplitudes within the parameter space (U, P_a). A comparison reveals that the primary resonance region ($U \approx 1$) exhibits a broad "V-shaped" resonance ridge with relatively gentle gradients, indicating that the response is relatively insensitive to moderate detuning from the exact resonance speed. In the primary resonance region [Figs. 5(a) and 5(b)], the morphologies of the surface elevation and velocity potential are highly consistent, both dominated by the direct resonance effect. Upon careful observation, it can be seen that the contour lines in the subcritical resonance region (to the left of the resonance peak) are relatively smooth, indicating that the wave height and velocity potential are essentially governed by the single factor of detuning. In contrast, the contour lines in the supercritical resonance region (to the right of the resonance peak) exhibit a distinct trend of bending or even turning back, suggesting that when the forced wave is under moderately nonlinear and strongly nonlinear wave conditions, the wave motion is subject to more complex governing factors. To identify and quantify the influencing factors in this region, we will calculate and analyze its discrete spectrum in the next part.

C. Cross-order interactions in resonance

As described in Sec. III B, the "deviation" filters out the background field of the free wave, thereby investigating the extent to which the forced wave system departs from its original state under external excitation. To deeply reveal the discrete spectrum laws within this forced disturbance, Figs. 6 and 7 present the amplitude contours of the first four harmonics for the surface elevation ($|a_1|$ to $|a_4|$) and the velocity potential ($|\alpha_1|$ to $|\alpha_4|$), respectively, in the (U, P_a) parameter space near the primary resonance region.

A comparison across the harmonic orders reveals clearly nonuniform evolution characteristics within the discrete spectrum. The fundamental modes ($|a_1|$ and $|\alpha_1|$) exhibit sharply defined "resonance ridge" features localized near the linear critical speed $U = 1.0$. In this region, the amplitudes first surge to a peak and subsequently decay as the detuning speed increases. However, a qualitatively different trend emerges in the higher-order harmonics ($j \geq 3$). As shown in Figs. 6(c), 6(d), 7(c), and 7(d), the resonance peak at $U = 1.0$ is smoothed out. Conversely, as the load moving speed U increases toward the right side of the parameter space, the amplitudes of the third and fourth harmonics ($|a_3|, |a_4|$ and $|\alpha_3|, |\alpha_4|$) demonstrate monotonic growth, with their maximum intensities concentrated in the high-speed, high-forcing regions.

For the fundamental harmonic, under external driving, when $U \approx 1.0$, the spatial frequency of the external load matches the natural frequency of the linear unperturbed solution, making the phase detuning minimal ($1 - U^2 \approx 0$). This direct resonance leads to localized amplification of the forced disturbance. Once the

02 September 2026 00:36:10

Published under an exclusive license by AIP Publishing

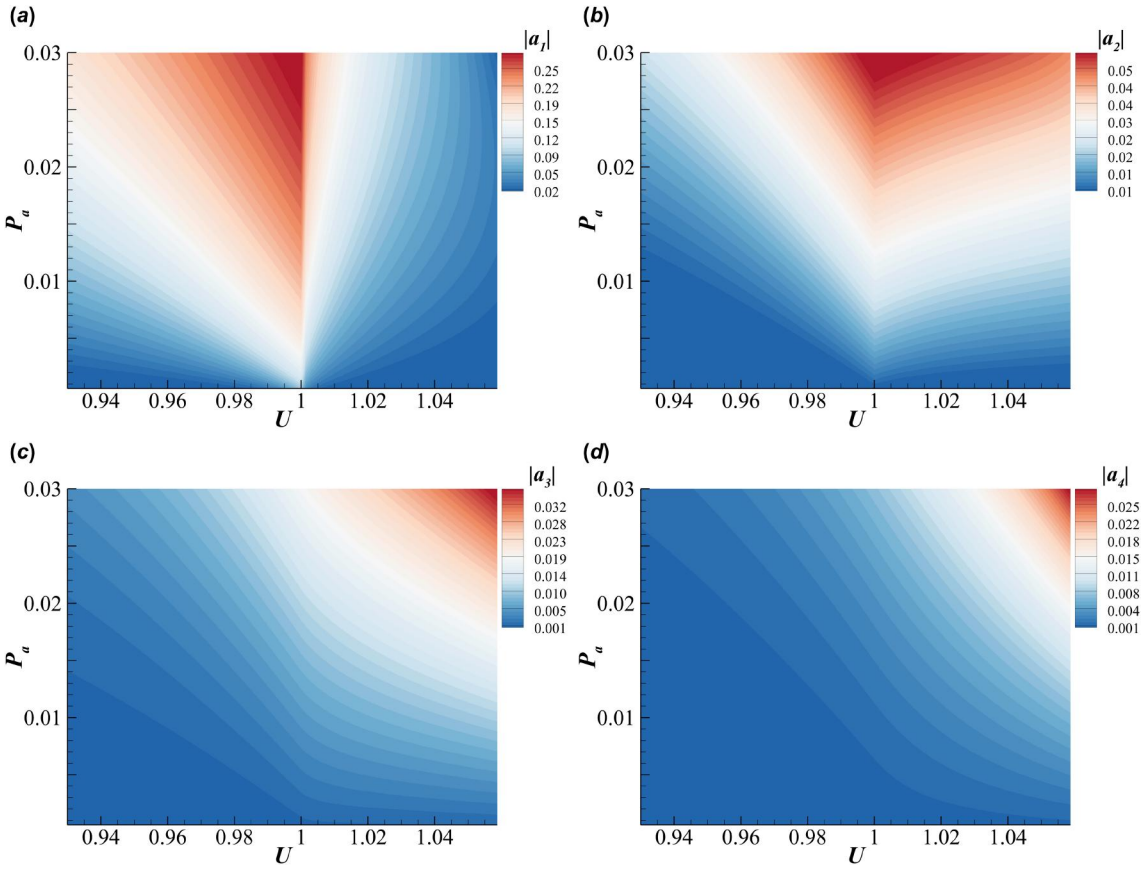

FIG. 6. Contour plots of the deviation harmonic amplitudes $|a_n|$ in the parameter space of load moving speed U and forcing amplitude P_a in the primary resonance region.

speed deviates from $U = 1.0$, the increasing detuning effect rapidly suppresses this direct energy absorption, thereby forming a sharp resonance ridge.

In Stark contrast, the higher-order components ($j \geq 3$) of the deviation are not primarily driven by the macroscopic external pressure. Within the conservative fluid domain, they exist as "bound waves," dynamically generated and maintained by cross-order nonlinear interactions of lower-order modes. When the prescribed wave speed U traverses past the linear critical point and continues to increase ($U > 1.0$), the wave system must climb higher along the nonlinear dispersion curve to sustain the required phase speed. This macroscopic kinematic requirement dictates rapid and highly nonlinear steepening of the background wave (unperturbed solution). Since the higher-order components of the background wave grow exponentially (or in high-power laws for Stokes waves) with the increasing wave steepness, this intense background nonlinear distortion acts as an additional nonlinear source of excitation. For the higher-order deviation, this explosive growth of the background nonlinearity is transmitted to the deviation through cross-order nonlinear interactions, largely masking the localized primary resonance effect occurring at $U = 1.0$, thereby dominating their continuous monotonic amplification at higher wave speeds. This disparity in the internal driving mechanisms suggests a structured cross-order coupling pattern within the forced wave system.

It is noteworthy that at high load speeds U, the amplitudes of the higher-order harmonics in the deviation approach or even exceed the amplitude of the fundamental wave. At this point, the higher-order harmonics in the deviation are entirely non-negligible, and their evolution laws and mechanisms are far more important than those near $U = 1$. In the following, we start with the higher-order harmonics of the velocity potential to analyze how the cross-order nonlinear interaction between the background wave and the deviation is transmitted under moderate-to-strong nonlinear wave conditions.

To quantify the discrete-spectrum distribution of the velocity potential within the primary resonance region, we extracted the evolution equations for the higher-order harmonics of the velocity potential of the deviation based on the high-precision numerical solutions obtained via MDDiM and the associated data. First, in the actual physical space

$$C_j = \frac{\hat{P}_a}{\rho} \cdot \left| \frac{\hat{\alpha}_{j-1}^{\langle s \rangle}}{\hat{\alpha}_j^{\langle e \rangle}} \right| \cdot \left| \frac{1}{\left[2k(\hat{A}^{\langle s \rangle})^2 + \frac{1}{k} \right] g - j\hat{U}^2} \right|. \tag{23}$$

Published under an exclusive license by AIP Publishing

02 September 2026 00:36:10

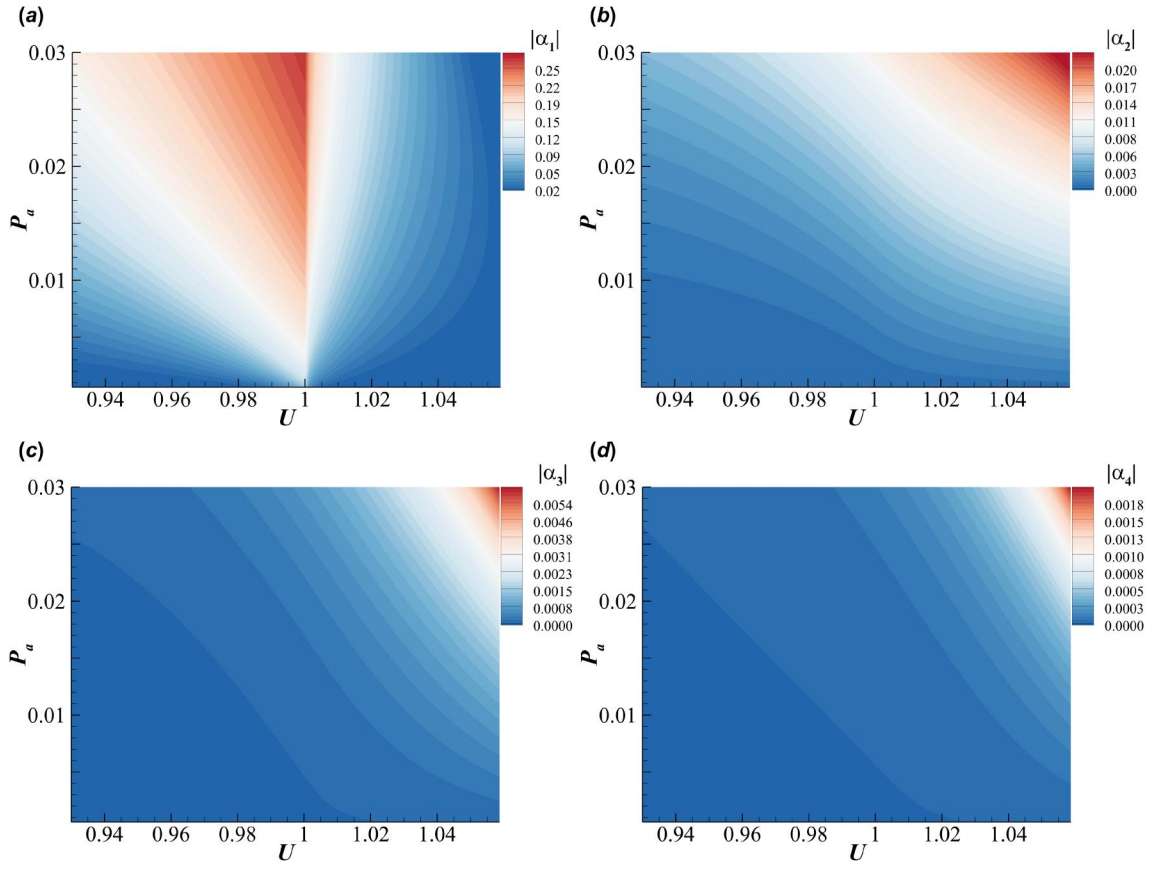

FIG. 7. The figure illustrates the distributions of the velocity potential amplitudes $|\alpha_j|$ of the deviation harmonics within the parameter space of load moving speed U and forcing amplitude P_a in the primary resonance region.

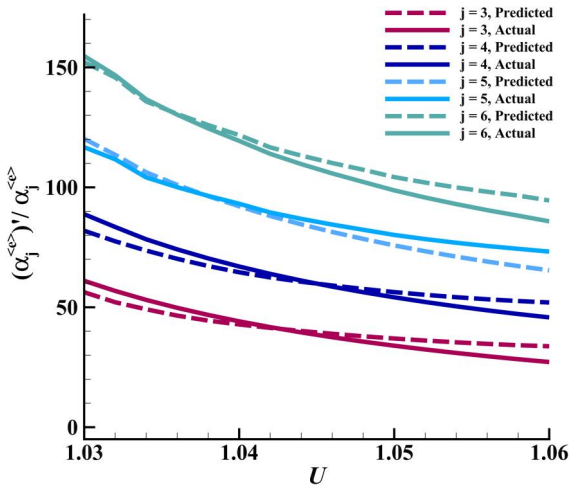

FIG. 8. Comparison of $(\alpha_j^{\langle e\rangle})'/\alpha_j^{\langle e\rangle}$ between Eq. (27) and actual data with errors within 9% and consistent decreasing trends (under moderate-to-strong nonlinear oscillations).

In this formula, the variables represent real physical quantities: $\hat{P}_a$ is the amplitude of the external moving pressure field, ρ is the fluid density, $\hat{U}$ is the moving speed of the pressure field, g is the gravitational acceleration, and k is the wavenumber; $\hat{\alpha}_j^{\langle e\rangle}$ represents the jth order Fourier coefficient of the velocity potential of the deviation, while $\hat{\alpha}_{j-1}^{\langle s\rangle}$ is the $(j-1)$ th order coefficient of the velocity potential of the corresponding background wave (unperturbed solution) (i.e., the free wave at the same phase speed), $\hat{A}^{\langle s\rangle}$ is the amplitude of the background wave (unperturbed solution) under the wave speed $\hat{U}$ and pressure $\hat{P}_a$, and C_j is a dimensionless number. On this basis, through nondimensionalization, we obtained an empirical relation applicable to weak excitation in the moderately strong and strongly nonlinear regime:

$$C_j = \left|\frac{P_a}{1 - jU^2 + 2\left(A^{\langle s\rangle}\right)^2}\right| \cdot \left|\frac{\alpha_{j-1}^{\langle s\rangle}}{\alpha_j^{\langle e\rangle}}\right|, \tag{24}$$

where $U = \hat{U}/\sqrt{g/k}$, $P_a = \hat{P}_a k/\rho g$, $\alpha_j^{\langle e\rangle} = k\hat{\alpha}_j^{\langle e\rangle}$, $\alpha_j^{\langle s\rangle} = k\hat{\alpha}_j^{\langle s\rangle}$, and $\hat{A}^{\langle s\rangle} = kA^{\langle s\rangle}$. The aforementioned equation is intended for moderately strong and strongly nonlinear forced waves under weak

02 September 2026 00:36:10

Published under an exclusive license by AIP Publishing

excitation. When the external excitation is larger, this relation may be extended to a form containing a general function $G_j(P_a)$:

$$C_j = \left| \frac{G_j(P_a)}{1 - jU^2 + 2(A^{\langle s \rangle})^2} \right| \cdot \left| \frac{\alpha_{j-1}^{\langle s \rangle}}{\alpha_j^{\langle e \rangle}} \right|. \tag{25}$$

It should be pointed out that the applicable range of this equation has certain physical boundaries: it is primarily applicable to the evolution of higher-order harmonics with order $j \geq 2$ and corresponds to moderately strong to strongly nonlinear waves with a dimensionless speed $1.03 < U < 1.07$ (wave steepness H_L approximately between 0.075 and 0.12). This velocity range was approximately determined through an MDDiM-based parameter sweep by requiring the coefficient of variation of C_j to remain below 7.5%. Typically, a $CV < 10\%$ signifies that the conservation law is fundamentally satisfied, whereas a $CV < 7.5\%$ confirms a high degree of conservation integrity. In weakly nonlinear waves, because the background wave (unperturbed solution) velocity potential component $\alpha_{j-1}^{\langle s \rangle}$ is relatively weak, it is no longer the dominant factor guiding the evolution of higher-order modes in the deviation; the cross-order interaction relationship may also be influenced by other nonlinear effects, which consequently leads to corresponding inaccuracies in this formula. Furthermore, excessive nonlinear distortion (approaching the limiting wave) introduces greater errors into the equations; therefore, the range of applicability is restricted to moderate-to-strong nonlinear waves under small loads.

According to the results in Tables III and IV, under the applicable conditions of the equations, although different wave speeds U and pressure amplitudes P_a cause significant changes in the overall wave profile and the amplitude levels of the velocity potential in the flow field, where P_a varies by two orders of magnitude, and the variables in the equations induced by U (such as the relevant amplitudes of the background wave (unperturbed solution) $\alpha_j^{\langle s \rangle}$, etc.) exhibit variation amplitudes ranging from several to dozens of times (Table IV), the Coefficient of Variation (CV) of C_j for a specific order j consistently remains at a low level below 5% (Table III). That is, within the applicable range, the values of C_j remain nearly constant within the tested parameter range, suggesting that Eqs. (23)–(25) capture a robust scaling relation in the nonlinear process.

The main physical significance of these equations is that they provide a robust scaling relation for the discrete-spectrum distribution of the deviation velocity potential in the moderate-to-strong nonlinear regime. Specifically, the dimensionless coefficient C_j compactly characterizes the coupling among the external excitation P_a, the adjacent lower-order component of the background-wave velocity potential $|\alpha_{j-1}^{\langle s \rangle}|$, the j-th order component of the deviation velocity potential $|\alpha_j^{\langle e \rangle}|$, and the nonlinear detuning term $|1 - jU^2 + 2(A^{\langle s \rangle})^2|$. The near constancy of C_j under variations in U and P_a within the tested weak excitation regime indicates that these four quantities are linked by an approximately invariant nonlinear constraint governing the cross-order spectral evolution.

To further elucidate the physical driving mechanism of each order's spectral component of the deviation velocity potential, the dimensionless equation can be algebraically reconstructed to obtain

$$\alpha_j^{\langle e \rangle} = \frac{1}{C_j} \cdot \left| \frac{P_a}{1 - jU^2 + 2(A^{\langle s \rangle})^2} \right| \cdot \alpha_{j-1}^{\langle s \rangle}. \tag{26}$$

This relationship indicates that the higher-order response $\alpha_j^{\langle e \rangle}$ of the deviation velocity potential is the result of a synergistic interaction among three factors: the external forcing scale P_a, the system's local nonlinear detuning, and the adjacent-order component $|\alpha_{j-1}^{\langle s \rangle}|$ of the background wave (unperturbed solution) velocity potential. Most notably, among these is the direct correlation presented between $|\alpha_j^{\langle e \rangle}|$ and $|\alpha_{j-1}^{\langle s \rangle}|$. This reflects that the higher-order deviation response induced by the external pressure field is largely controlled by the strength of the adjacent lower-order spectral component $\alpha_{j-1}^{\langle s \rangle}$ in the corresponding background flow field. When the flow field is in a moderately strong or strongly nonlinear stage, the background wave (unperturbed solution) undergoes significant steepening, and its higher-order velocity potential component $\alpha_{j-1}^{\langle s \rangle}$ escalates sharply; the evolution of this state promotes the corresponding amplification of the deviation spectral component $\alpha_j^{\langle e \rangle}$ through cross-order interactions. Simultaneously, the denominator of the equation participates in this process as a regulatory mechanism, wherein the classical linear dispersion detuning $1 - jU^2$ provides the fundamental kinematic phase mismatch, while the nonlinear frequency shift $2A^{\langle s \rangle}$ induced by the background-wave amplitude applies a moderate dynamic correction to this detuning.

Furthermore, Eq. (26) can also be regarded as providing a rapid estimation method for the high-order discrete spectra of forced waves. Since the background wave $\phi_{\text{intrinsic}}$ is explicitly known (i.e., a free Stokes nonlinear wave), as long as the external excitation P_a and the load moving speed U are provided as inputs, the various order components in the deviation velocity potential can be directly calculated to obtain ϕ_{excited}, and subsequently, the high-order discrete-spectrum distribution of the total velocity potential for the forced wave can be approximately obtained according to $\phi_{\text{total}} = \phi_{\text{excited}} + \phi_{\text{intrinsic}}$.

By taking the natural logarithm of Eq. (26) and subsequently differentiating it with respect to U, we obtain

$$\frac{(\alpha_j^{\langle e \rangle})'}{\alpha_j^{\langle e \rangle}} \approx \frac{(\alpha_{j-1}^{\langle s \rangle})'}{\alpha_{j-1}^{\langle s \rangle}} + \frac{2jU - 4A^{\langle s \rangle}(A^{\langle s \rangle})'}{1 - jU^2 + 2(A^{\langle s \rangle})^2}, \tag{27}$$

where the prime symbol ($'$) denotes the derivative with respect to the load moving speed U, while $(\alpha_j^{\langle e \rangle})'/\alpha_j^{\langle e \rangle}$ and $(\alpha_{j-1}^{\langle s \rangle})'/\alpha_{j-1}^{\langle s \rangle}$ represent the growth rates of the jth order harmonic amplitude of the deviation velocity potential and the $(j-1)$ th order harmonic amplitude of the background-wave velocity potential, respectively. A crucial observation here is that the amplitude and the growth rate of the jth order deviation are directly governed by the adjacent lower-order $(j-1)$ th component of the background wave. This structured cross-order coupling is noteworthy, suggesting a hierarchical sequence in the internal energy distribution.

As illustrated in Fig. 8, the predicted values derived from Eq. (27) exhibit good agreement with the actual data, with the calculation error remaining within 9% under moderate-to-strong nonlinear oscillations. This close alignment quantitatively validates the rationality and accuracy of the proposed analytical formulation, Eqs. (23)–(27), which captures the dominant factors governing the evolution of deviations under moderate-to-strong nonlinear conditions. Furthermore, the trends in Fig. 8 indicate that the growth rate of the amplitude decreases monotonically as the load moving speed U increases.

02 September 2026 00:36:10

Published under an exclusive license by AIP Publishing

TABLE III. Comparison of the dimensionless coefficients C_j for various load speeds U and external small pressure amplitudes P_a, calculated by solving the original governing equations using MDDiM. The last row represents the Coefficient of Variation (CV) for each column. Here, $G_j(P_a) = P_a$ and $p_0 = 10^{-4}$ are adopted, with C_j computed via Eq. (24).

Parameters	C_2	C_3	C_4	C_5	C_6
$U = 1.035, P_a = 0.1p_0$	0.604 845	0.049 2684	0.017 6584	0.009 778 49	0.005 949 61
$U = 1.045, P_a = 0.1p_0$	0.585 658	0.052 0673	0.018 6432	0.009 959 12	0.005 995 52
$U = 1.050, P_a = 0.1p_0$	0.575 613	0.052 6324	0.018 7993	0.009 900 09	0.005 927 7
$U = 1.055, P_a = 0.1p_0$	0.565 166	0.052 7227	0.018 7612	0.009 755 14	0.005 809 22
$U = 1.065, P_a = 0.1p_0$	0.542 429	0.051 5475	0.018 1547	0.009 286 02	0.005 516 77
$U = 1.035, P_a = p_0$	0.604 015	0.049 0785	0.017 5483	0.009 687 91	0.005 878 1
$U = 1.045, P_a = p_0$	0.585 032	0.051 899	0.018 5499	0.009 886 37	0.005 939 03
$U = 1.050, P_a = p_0$	0.575 053	0.052 4734	0.018 7124	0.009 833 95	0.005 876 77
$U = 1.055, P_a = p_0$	0.564 657	0.052 5719	0.018 6798	0.009 694 5	0.005 762 96
$U = 1.065, P_a = p_0$	0.541 987	0.051 4092	0.018 0814	0.009 233 24	0.005 476 82
$U = 1.035, P_a = 5p_0$	0.600 364	0.048 2431	0.017 0693	0.009 296 41	0.005 570 8
$U = 1.045, P_a = 5p_0$	0.582 269	0.051 1573	0.018 1412	0.009 569 52	0.005 694 03
$U = 1.050, P_a = 5p_0$	0.572 579	0.051 7721	0.018 3311	0.009 545 06	0.005 655 24
$U = 1.055, P_a = 5p_0$	0.562 404	0.051 9061	0.018 3217	0.009 429 06	0.005 561 22
$U = 1.065, P_a = 5p_0$	0.540 025	0.050 7975	0.017 7583	0.009 001 43	0.005 301 97
$U = 1.035, P_a = 10p_0$	0.595 89	0.047 2191	0.016 4932	0.008 831 46	0.005 209 8
$U = 1.045, P_a = 10p_0$	0.578 86	0.050 2449	0.017 6439	0.009 187 85	0.005 401 35
$U = 1.050, P_a = 10p_0$	0.569 517	0.050 908	0.017 8653	0.009 195 4	0.005 389 1
$U = 1.055, P_a = 10p_0$	0.559 61	0.051 0842	0.017 883	0.009 106 54	0.005 317 78
$U = 1.065, P_a = 10p_0$	0.537 58	0.050 0395	0.017 3602	0.008 717 96	0.005 289 48
CV error	3.66%	2.99%	3.43%	3.92%	4.56%

TABLE IV. Variation amplitudes of the variables in Eqs. (24) and (25) when given $P_a = p_0$, and the moving speed U varies within the range $1.035 < U < 1.065$. Judging from the CV values and the range ratios of the parameters, the input variables of the equations undergo significant variations, which further corroborates the reasonable stability of Eqs. (24) and (25).

Indicators of parameter changes	$(A^{\langle s\rangle})^2$	$\alpha_2^{\langle s\rangle}$	$\alpha_3^{\langle s\rangle}$	$\alpha_4^{\langle s\rangle}$	$\alpha_5^{\langle s\rangle}$
CV of parameter variation	47.63%	83.42%	108.27%	124.35%	133.26%
Range ratio of parameter variation (max/min)	2.0	3.9	7.6	15.6	33.7

Simultaneously, higher-order modes (larger j values) consistently demonstrate higher baseline growth rates, further corroborating the hierarchical sequence of internal energy distribution dominated by adjacent lower-order components as described by the formula.

Although Eqs. (26) and (27) are derived under conditions of small load and moderate-to-strong nonlinear wave motion, the trends and basic laws they express remain valid for large loads according to the results of MDDiM (Fig. 7), despite the discrepancy between the predicted results and the actual calculations from MDDiM will increase.

IV. CONCLUSIONS

Within the framework of the homotopy analysis method (HAM), this paper generalizes the application of MDDiM in resolving the small-divisor problem to the realm of partial differential equations by defining new auxiliary inverse operators. On the basis of efficiently capturing multiple steady-state solution branches of strongly nonlinear forced responses, this work systematically elucidates the primary resonance bifurcation characteristics and cross-order coupling cascade mechanisms of deep-water forced waves. The main conclusions are summarized as follows:

(1) An efficient MDDiM-based algorithm for solving strongly nonlinear problems is developed. By defining two classes of new auxiliary linear inverse operators, the small-divisor difficulty inherent in traditional perturbation theories is effectively addressed. Compared to singular perturbation methods such as the method of multiple scales (MMSs), MDDiM eliminates the need for tedious scale analysis for different parameter groups, features a more concise algorithm, and does not rely on the "weak nonlinearity" assumption of small parameters. The proposed method shows good robustness and practical usability in solving strongly nonlinear problems, and it captures multiple steady-state solution branches in the forced response with good accuracy.

02 September 2026 00:36:10

Published under an exclusive license by AIP Publishing

(2) The dynamical characteristics and bifurcation structure of deep-water forced waves in the primary resonance region are examined and interpreted. The results indicate that, due to the "hard-spring" characteristics of the nonlinear dispersion of deep-water waves, the forced-response branches of the system tilt to the right, thereby triggering fold bifurcations. This quantitatively characterizes the multi-steady-state jump behavior of the forced wave system under strong resonance conditions.
(3) The cross-order coupling mechanism between the deviation response and the background wave is identified and quantitatively characterized. Through an in-depth analysis of the discrete spectra, an analytical equation describing the moderate-to-strong nonlinear forced evolution stage is established, which quantitatively characterizes the evolution rules of the harmonic amplitudes of the velocity potential of the deviation. The results demonstrate that higher-order deviation responses do not evolve independently but are strongly modulated by adjacent lower-order background-wave components; the nonlinear steepening of the background wave essentially constitutes an important parametric excitation source driving the higher-order deviation responses. The proposed "structured cascade sequence model" quantitatively reflects the influence of the growth rate of adjacent lower-order components in the background wave on the growth rate of higher-order deviation responses, providing a useful physical picture for understanding cross-order coupling mechanisms in forced nonlinear wave–wave interactions.

Future studies will investigate more bifurcation phenomena of steady periodic gravity waves and the possibility of obtaining non-Stokes branches by introducing more efficient basis functions for extremely nonlinear waves. Harmonic resonance regimes beyond the primary resonance considered here will also be examined. In addition, more systematic criteria for defining auxiliary inverse operators will be developed, and the MDDiM framework will be extended to other nonlinear free-surface problems.

SUPPLEMENTARY MATERIAL

See the supplementary material for additional derivations for the MDDiM formulation, details of the numerical implementation, and supporting validation data and figures.

ACKNOWLEDGMENTS

This work was partly supported by the National Natural Science Foundation of China (Nos. 12272230 and 12521002).

AUTHOR DECLARATIONS

Conflict of Interest

The authors have no conflicts to disclose.

Author Contributions

Danshi Zhao: Data curation (lead); Investigation (lead); Methodology (lead); Software (lead); Writing – original draft (lead). **Shijun Liao:** Conceptualization (lead); Funding acquisition (lead); Supervision (lead); Writing – review & editing (lead).

DATA AVAILABILITY

The data that support the findings of this study are available from the corresponding author upon reasonable request.

APPENDIX: MATHEMATICAL DEFINITIONS OF THE OPERATORS AND EXPRESSIONS

The i-th order deformation components ϕ_i and ξ_i of the velocity potential and wave surface elevation are fundamentally defined as the i-th order Taylor expansion coefficients of the homotopy mapping functions with respect to the embedding parameter q at $q = 0$:

$$\phi_i(x,y) = \frac{1}{i!}\frac{\partial^i \Phi(x,y,q)}{\partial q^i}\bigg|_{q=0}, \tag{A1}$$

$$\xi_i(x) = \frac{1}{i!}\frac{\partial^i \Theta(x,q)}{\partial q^i}\bigg|_{q=0}. \tag{A2}$$

During the continuous deformation process, the total derivative operator D/Dq on the moving boundary $y = \Theta(x,q)$, which represents the material derivative tracking the deformation of the free surface, obeys the following elementary mathematical relation:

$$\frac{D\Phi(x,y,q)}{Dq} = \frac{\partial \Phi(x,y,q)}{\partial q} + \frac{\partial \Theta(x,q)}{\partial q}\frac{\partial \Phi(x,y,q)}{\partial y} \quad \text{at } y = \Theta(x,q). \tag{A3}$$

The ith order nonlinear residual terms $\mathscr{R}_i^{\phi}(x)$ and $\mathscr{R}_i^{\xi}(x)$ are defined as the ith order total derivatives of the original nonlinear operators with respect to q evaluated at the initial state $q = 0$:

$$\mathscr{R}_i^{\phi}(x) = \frac{1}{i!}\frac{D^i \mathscr{N}_{\phi}\left[\Phi(x,\Theta,q)\right]}{Dq^i}\bigg|_{q=0}, \tag{A4}$$

$$\mathscr{R}_i^{\xi}(x) = \frac{1}{i!}\frac{D^i \mathscr{N}_{\xi}\left[\Phi(x,\Theta,q),\Theta(x,q)\right]}{Dq^i}\bigg|_{q=0}. \tag{A5}$$

Furthermore, the ith order total derivative of the mapping Φ expanded at the mean water level $y = 0$ can be written as

$$\frac{1}{i!}\frac{D^i \Phi(x,\Theta,q)}{Dq^i}\bigg|_{q=0} = \phi_i|_{y=0} + \mathscr{B}_i^{(1)}[\vec{\phi}_i, \vec{\xi}_i], \tag{A6}$$

where the history solution vectors are defined as $\vec{\phi}_i = (\phi_0, \phi_1, \ldots, \phi_{i-1})$ and $\vec{\xi}_i = (\xi_1, \xi_2, \ldots, \xi_{i-1})$. To map the boundary conditions strictly to $y = 0$, we introduce the high-order boundary evolution operator $\mathscr{B}_i^{(z_n)}$, which fundamentally combines the Taylor series expansions with the Faà di Bruno formula for high-order chain rules of composite functions:

$$\mathscr{B}_i^{(z_n)}[\vec{\phi}_i, \vec{\xi}_i] = \sum_{m=1}^{i}\sum_{n=0}^{i-m}\frac{z_n}{m!(i-n)!}\frac{\partial^m \phi_n}{\partial y^m}\bigg|_{y=0} \cdot \frac{\partial^{i-n}}{\partial q^{i-n}}\left(\sum_{r=1}^{i-n-m+1}\xi_r(x)q^r\right)^m\bigg|_{q=0}. \tag{A7}$$

Accordingly, the high-order polynomial correction term $\mathscr{T}_i$ used to modify the boundary operator values during deformation

02 September 2026 00:36:10

Published under an exclusive license by AIP Publishing

is explicitly derived by substituting the specific weights $z_n = \chi_{n+1}$ into the boundary evolution operator:

$$\mathscr{T}_i = \sum_{m=1}^{i} \sum_{n=0}^{i-m} \frac{\chi_{n+1}}{m!(i-n)!} \frac{\partial^m \mathscr{L}[\phi_n]}{\partial y^m}\bigg|_{y=0} \cdot \frac{\partial^{i-n}}{\partial q^{i-n}} \left(\sum_{r=1}^{i-n-m+1} \xi_r(x) q^r \right)^m \bigg|_{q=0}. \tag{A8}$$

By definition, if the upper bound of a summation is less than its lower bound, the summation equals zero, which naturally yields the initial value $\mathscr{T}_0 = 0$.

REFERENCES

[1]L. J. Doctors and S. D. Sharma, "The wave resistance of an air-cushion vehicle in steady and accelerated motion," J. Ship Res. **16**, 248–260 (1972).
[2]K. J. Maki, R. Broglia, L. J. Doctors, and A. Di Mascio, "Nonlinear wave resistance of a two-dimensional pressure patch moving on a free surface," Ocean Eng. **39**, 62–71 (2012).
[3]T. R. Akylas, "On the excitation of long nonlinear water waves by a moving pressure distribution," J. Fluid Mech. **141**, 455–466 (1984).
[4]R. C. Ertekin, W. C. Webster, and J. V. Wehausen, "Waves caused by a moving disturbance in a shallow channel of finite width," J. Fluid Mech. **169**, 275–292 (1986).
[5]T. Y.-T. Wu, "Generation of upstream advancing solitons by moving disturbances," J. Fluid Mech. **184**, 75–99 (1987).
[6]D. B. Ersan and S. Beji, "Numerical simulation of waves generated by a moving pressure field," Ocean Eng. **59**, 231–239 (2013).
[7]L. J. Doctors and G. Dagan, "Comparison of nonlinear wave-resistance theories for a two-dimensional pressure distribution," J. Fluid Mech. **98**, 647–672 (1980).
[8]E. Părău and F. Dias, "Nonlinear effects in the response of a floating ice plate to a moving load," J. Fluid Mech. **460**, 281–305 (2002).
[9]A. V. Pogorelova and V. M. Kozin, "Flexural-gravity waves due to unsteady motion of point source under a floating plate in fluid of finite depth," J. Hydrodyn. **22**, 71–76 (2010).
[10]Z. Wang, "A universal bifurcation mechanism arising from progressive hydroelastic waves," Theor. Appl. Mech. Lett. **12**(1), 100315 (2022).
[11]Z. Wang, J. M. Vanden-Broeck, and P. A. Milewski, "Two-dimensional flexural–gravity waves of finite amplitude in deep water," IMA J. Appl. Math. **78**, 750–761 (2013).
[12]P. A. Milewski, J. M. Vanden-Broeck, and Z. Wang, "Steady dark solitary flexural gravity waves," Proc. R. Soc. A **469**, 20120485 (2013).
[13]T. Gao, Z. Wang, and J.-M. Vanden-Broeck, "New hydroelastic solitary waves in deep water and their dynamics," J. Fluid Mech. **788**, 469–491 (2016).
[14]R. H. J. Grimshaw and N. Smyth, "Resonant flow of a stratified fluid over topography," J. Fluid Mech. **169**, 429–464 (1986).
[15]O. M. Phillips, "On the generation of waves by turbulent wind," J. Fluid Mech. **2**, 417–445 (1957).
[16]M. Paprota, "On pressure forcing techniques for numerical modelling of unidirectional nonlinear water waves," Appl. Ocean Res. **90**, 101857 (2019).
[17]G. G. Dogan, E. Pelinovsky, A. Zaytsev, A. D. Metin, G. O. Tarakcioglu, A. C. Yalciner, B. Yalciner, and I. Didenkulova, "Long wave generation and coastal amplification due to propagating atmospheric pressure disturbances," Nat. Hazards **106**, 1195–1221 (2021).
[18]T. Kakinuma, "Tsunamis generated and amplified by atmospheric pressure waves due to an eruption over seabed topography," Geosciences **12**, 232 (2022).
[19]T. Kakinuma and J. Kosugi, "Numerical study on the excitation and propagation of surface/internal waves due to air pressure waves over topography," Water Waves **7**, 315–348 (2025).
[20]F. Zhu and Z-m Yuan, "Wave drag and wave patterns by ships moving in a single-file formation," Phys. Fluids **36**, 061910 (2024).
[21]E. I. Părău and J.-M. Vanden-Broeck, "Nonlinear two-and three-dimensional free surface flows due to moving disturbances," Eur. J. Mech.-B/Fluids **21**, 643–656 (2002).
[22]T. R. Akylas, "On the excitation of nonlinear water waves by a moving pressure distribution oscillating at resonant frequency," Phys. Fluids **27**, 2803–2807 (1984).
[23]O. M. Phillips, "On the dynamics of unsteady gravity waves of finite amplitude. Part 1. The elementary interactions," J. Fluid Mech. **9**, 193–217 (1960).
[24]K. Hasselmann, "On the non-linear energy transfer in a gravity-wave spectrum. Part 1. General theory," J. Fluid Mech. **12**, 481–500 (1962).
[25]D. M. Kouskoulas and Y. Toledo, "Deep water gravity wave triad resonances on uniform flow," Phys. Fluids **32**, 076603 (2020).
[26]H. C. Yuen and B. M. Lake, "Nonlinear dynamics of deep-water gravity waves," Adv. Appl. Mech. **22**, 67–229 (1982).
[27]V. P. Krasitskii, "On reduced equations in the Hamiltonian theory of weakly nonlinear surface waves," J. Fluid Mech. **272**, 1–20 (1994).
[28]Z. Liu and D. Xie, "Finite-amplitude steady-state wave groups with multiple near-resonances in finite water depth," J. Fluid Mech. **867**, 348–373 (2019).
[29]S. J. Liao, "On the homotopy multiple-variable method and its applications in the interactions of nonlinear gravity waves," Commun. Nonlinear Sci. Numer. Simul. **16**, 1274–1303 (2011).
[30]N. Masnadi and J. H. Duncan, "The generation of gravity–capillary solitary waves by a pressure source moving at a trans-critical speed," J. Fluid Mech. **810**, 448–134 (2017).
[31]R. Pethiyagoda, S. W. McCue, and T. J. Moroney, "What is the apparent angle of a kelvin ship wave pattern?," J. Fluid Mech. **758**, 468–485 (2014).
[32]A. Darmon, M. Benzaquen, and E. Raphaël, "Kelvin wake pattern at large Froude numbers," J. Fluid Mech. **738**(3), R3 (2014).
[33]A. M. Reed and J. H. Milgram, "Ship wakes and their radar images," Annu. Rev. Fluid Mech. **34**, 469–502 (2002).
[34]T. Zdyrski and F. Feddersen, "Wind-induced changes to surface gravity wave shape in deep to intermediate water," J. Fluid Mech. **903**, A31 (2020).
[35]A. Giorgilli *et al.*, "Small denominators and exponential stability: From Poincaré to the present time," Semin. Mat. Fis. Milano **68**, 19–57 (1998).
[36]H. Poincaré, *Les Méthodes Nouvelles de la Mécanique Céleste* (Gauthier-Villars et fils, imprimeurs-libraires, 1893), Vol. 2.
[37]C. Delaunay, *Théorie du Mouvement de la Lune* (Mallet-Bachelier, 1867), Vol. 28.
[38]A. N. Kolmogorov, "On conservation of conditionally periodic motions for a small change in Hamilton's function," Dokl. Akad. Nauk Sssr **98**, 527–530 (1954).
[39]R. A. Pérez, "A brief but historic article of Siegel," Not. Am. Math. Soc. **58**, 558–566 (2011).
[40]A. H. Nayfeh and D. T. Mook, *Nonlinear Oscillations* (John Wiley & Sons, New York, 1979).
[41]A. H. Nayfeh, *Introduction to Perturbation Techniques* (John Wiley & Sons, New York, 1981).
[42]D. G. Dommermuth and D. K. P. Yue, "A high-order spectral method for the study of nonlinear gravity waves," J. Fluid Mech. **184**, 267–288 (1987).
[43]B. Cochelin and C. Vergez, "A high order purely frequency-based harmonic balance formulation for continuation of periodic solutions," J. Sound Vib. **324**, 243–262 (2009).
[44]S. Liao, "On the homotopy analysis method for nonlinear problems," Appl. Math. Comput. **147**(2), 499–513 (2004).
[45]S. Liao and Y. Tan, "A general approach to obtain series solutions of nonlinear differential equations," Stud. Appl. Math. **119**, 297–354 (2007).
[46]S. Liao, "Notes on the homotopy analysis method: Some definitions and theorems," Commun. Nonlinear Sci. Numer. Simul. **14**, 983–997 (2009).
[47]S. Liao, "An optimal homotopy-analysis approach for strongly nonlinear differential equations," Commun. Nonlinear Sci. Numer. Simul. **15**, 2003–2016 (2010).
[48]D. Xu, Z. Lin, S. Liao, and M. Stiassnie, "On the steady-state fully resonant progressive waves in water of finite depth," J. Fluid Mech. **710**, 379–418 (2012).
[49]Z. Liu and S. J. Liao, "Steady-state resonance of multiple wave interactions in deep water," J. Fluid Mech. **742**, 664–700 (2014).

02 September 2026 00:36:10

Published under an exclusive license by AIP Publishing

[50]S. Liao, D. Xu, and M. Stiassnie, "On the steady-state nearly resonant waves," J. Fluid Mech. **794**, 175–199 (2016).
[51]Z. Liu, D. Xu, and S. Liao, "Finite amplitude steady-state wave groups with multiple near resonances in deep water," J. Fluid Mech. **835**, 624–653 (2018).
[52]X. Zhong and S. Liao, "On the limiting stokes wave of extreme height in arbitrary water depth," J. Fluid Mech. **843**, 653–679 (2018).
[53]X. Yang, F. Dias, Z. Liu, and S. Liao, "Finite-amplitude steady-state resonant waves in a circular basin," J. Fluid Mech. **915**, A136 (2021).
[54]J. Li, Z. Liu, S. Liao, and A. G. Borthwick, "Steady-state harmonic resonance of periodic interfacial waves with free-surface boundary conditions based on the homotopy analysis method," J. Fluid Mech. **916**, A58 (2021).
[55]S. Liao and Y. Zhao, "On the method of directly defining inverse mapping for nonlinear differential equations," Numer. Algorithm **72**, 989–1020 (2016).
[56]S. Liao, "Avoiding small denominator problems by means of the homotopy analysis method," arXiv:2208.04136 (2022).
[57]S. Liao, *Beyond Perturbation: Introduction to the Homotopy Analysis Method* (Chapman and Hall/CRC, Boca Raton, FL, 2003).
[58]L. W. Schwartz, "Computer extension and analytic continuation of Stokes' expansion for gravity waves," J. Fluid Mech. **62**, 553–578 (1974).
[59]M. S. Longuet-Higgins, "Integral properties of periodic gravity waves of finite amplitude," Proc. R. Soc. London, Ser. A **342**, 157–174 (1975).

02 September 2026 00:36:10

Published under an exclusive license by AIP Publishing